Correspondence to:
W. Duan,
duanws@lasg.iap.ac.cn

The Sensitive Area for Targeting Observations of Paired Mesoscale Eddies Associated With Sea Surface Height Anomaly Forecasts

Lin Jiang[1,2], Wansuo Duan[2,3] , and Hui Wang[1,4,5]

[1]Institute of Marine Science and Technology, Shandong University, Qingdao, China, [2]State Key Laboratory of Numerical Modeling for Atmospheric Sciences and Geophysical Fluid Dynamics (LASG), Institute of Atmospheric Physics, Chinese Academy of Sciences, Beijing, China, [3]Collaborative Innovation Center on Forecast and Evaluation of Meteorological Disasters (CIC-FEMD), Nanjing University of Information Science and Technology, Nanjing, China, [4]Southern Marine Science and Engineering Guangdong Laboratory, Zhuhai, China, [5]National Marine Environmental Forecasting Center, Beijing, China

Abstract For paired mesoscale eddies, the most sensitive initial errors in relation to sea surface height anomaly (SSHA) forecasts are investigated by utilizing the conditional nonlinear optimal perturbation (CNOP) method in a two-layer quasigeostrophic model and then the sensitive areas are identified accordingly. For counter-rotating eddies, the CNOP initial errors primarily occur within the eddies themselves, especially in areas characterized by clear high-to low-velocity gradients, accompanied by shear structures; while for co-rotating eddies, besides sharing the feature of the former, their CNOP initial errors also concentrate between the two eddies and are obliquely tangential to their boundaries with a positive and negative shear structure. The utility of the CNOP initial errors in determining the sensitive areas for target observation is assessed through observing system simulation experiments (OSSEs). The OSSEs indicate that giving priority to the implementation of target observations in the sensitive areas identified by large CNOP initial errors, whether within eddies or between two co-rotating eddies, particularly with a specific array guided by the shear structure of CNOP initial errors, leads to a notable improvement in SSHA forecasting. Finally, the effectiveness of the target observations, especially within the sensitive area situated between two co-rotating eddies, is interpreted from the perspective of barotropic instability. The results of this study offer valuable scientific insights into the targeted observation of paired mesoscale eddies. These findings have the potential to provide important guidance for initializating paired mesoscale eddies, ultimately contributing to improvements in SSHA forecast accuracy.

Plain Language Summary Sea surface height anomaly (SSHA) is a critical variable for describing ocean surface dynamics, and improving the accuracy of SSHA predictions is of utmost importance. Given that the initialization of mesoscale eddies plays a pivotal role in SSHA forecasts, and these eddies often appear in pairs in the world's oceans, we investigate the impact of paired mesoscale eddies on the sensitivity of SSHA forecasting. Our findings indicate that, for paired mesoscale eddies, in contrast to individual eddies, the sensitive areas associated with SSHA forecasting are not only confined to the eddies themselves, specifically the area within eddies characterized by a high-to low-velocity gradient, but also located between two eddies, especially in the case of co-rotating eddies. Targeting observations in these sensitive areas of paired mesoscale eddies, especially with a specific array, can significantly enhance the accuracy of SSHA forecasts. This improvement can be explained by the mechanism of barotropic instability. This research holds the potential to make a substantial contribution to the initialization of paired mesoscale eddies, consequently enhancing the precision of SSHA forecasts.

1. Introduction

Sea surface height anomaly (SSHA) is viewed as the foremost variable to describe ocean surface dynamics (Nicholls & Cazenave, 2010). The SSHA can exert substantial influence on the frequency and severity of extreme sea level events, and it is very concerned by ship navigation, fishery resource forecasting, marine engineering and industry (Lumban-Gaol et al., 2017; Tanajura et al., 2015). Therefore, accurate prediction of SSHA holds immense significance (Fraser et al., 2019).

Numerical models have been at the forefront of ocean forecasts for decades and are frequently employed for predicting SSHA. However, uncertainties in SSHA forecasting persist because of initial and model errors (Agarwal et al., 2022; Song et al., 2021); furthermore, the nonlinear instability of ocean fluid motion amplifies these uncertainties (Miao et al., 2023). With the realization of satellite technology, the altimeter provides SSHA observation data on a nearly global scale, and then assimilating these data becomes an effective way to reduce the uncertainty of SSHA prediction (Oke et al., 2013). It is worth noting that assimilating additional observations in regions highly sensitive to the initial values of forecasts leads to a significant improvement in forecasting skill; conversely, in areas with weak sensitivity, it may yield only modest improvements or, in certain instances, even poorer forecasting skills due to additional errors induced by imperfect assimilation procedures or unsolved processes in models (Janjic et al., 2018; Yang et al., 2023). Hence, even if there are sufficient observations, it remains crucial to prioritize the specific areas where the observations should be preferentially assimilated to attain better forecasting skills. It is therefore essential to identify the areas where the initial errors are most influential on the predictions of SSHA. Such argument is associated with an observational strategy known as "target observation" (Mu, 2013; Snyder, 1996). That is, to enhance the prediction of an event at a future time t_1 (referred to as the verification time) within a specific area of interest (referred to as the verification area), additional observations are strategically deployed at time t_2 (called the targeted time; typically $t_2 < t_1$) in some key areas (called the "sensitive area"), where the additional observations are expected to exert a significant impact on the forecasts within the verification area. By prioritizing the assimilation of targeted observations in sensitive areas, more dependable initial states can be formed, thereby reducing the prediction errors of concerned events much effectively.

It is known that the world's oceans are abundant with mesoscale eddies; in particular, the chaotic nature of such vortex-dominated turbulence is significantly controlled by the chaotic motion of eddies (Babiano et al., 1994). By using a two-layer quasigeostrophic (QG) model, Weiss and Grooms (2017) demonstrated that accurately initializing mesoscale eddies can improve the estimation and prediction of ocean states. In their study, they employed an assimilation strategy for mesoscale eddies by assimilating observations evenly distributed over the eddies, and the results indicated that this assimilation strategy is more effective in enhancing the forecasting performance of ocean states than assimilating only a portion of observations distributed on uniformly spaced grids across the entire model domain. However, mesoscale eddies typically have irregular shapes and asymmetric flow fields, which reduce vortex structure stability and introduce highly nonlinearity (Cheng et al., 2014; Wang et al., 2023). Taking this into consideration, Jiang et al. (2022) investigated the sensitivity of mesoscale eddies related to SSHA forecasts and unveiled the significance of this sensitivity in identifying sensitive areas for target observation. The investigation also utilized a two-layer QG model, akin to the one employed by Weiss and Grooms (2017). They found that there indeed exist sensitive areas on mesoscale eddies, which present strong sensitivity to initial errors of SSHA forecasting; more specifically, when additional observations are preferentially implemented in the sensitive area where the eddies present a clear high to low-velocity gradient along the eddy rotation, it significantly enhances the forecasting capability for SSHA (also see Jiang et al., 2023). Note that Jiang et al. (2022) paid attention to the sensitivity of SSHA forecasting on individual mesoscale eddy.

In practice, the oceanic mesoscale eddies frequently arise in pairs (as illustrated in Figure 1) and one of the hallmarks of ocean turbulence is eddy-eddy interaction (Harrison et al., 2013; Huang & Wang, 2022; Ni et al., 2020). Specifically, paired mesoscale eddies manifest in two distinct configurations: counter-rotating pairs and co-rotating pairs. Concerning counter-rotating pairs composed of an anticyclone and a cyclone, they are separated by a central jet, and noticeable gradients in density and temperature can be observed between two counter-rotating eddies (Durán-Campos et al., 2019; Pidcock et al., 2013); while regarding co-rotating pairs, which comprise either two anticyclones or two cyclones, they are generally recognized for featuring a relatively weak flow field within the interstice between two eddies. Previous studies demonstrated that paired eddies usually interact with each other, altering their motion parameters and geometric properties, leading to the redistribution of kinetic energy and the enhancement of eddy nonlinearity (Fedorov & Belonenko, 2020). Therefore, in relation to more practical scenarios, it is imperative to delve into the impact of initial uncertainties associated with paired mesoscale eddies on SSHA prediction. A more specific aspect pertains to target observations, prompting queries: where are the sensitive areas for target observation of paired mesoscale eddies in relation to SSHA forecasts? Are they different from those of individual eddies? What mechanism determines the sensitive areas of paired eddies? To address these issues, the two-layer QG model utilized in Jiang et al. (2022) is still adopted here, facilitating a
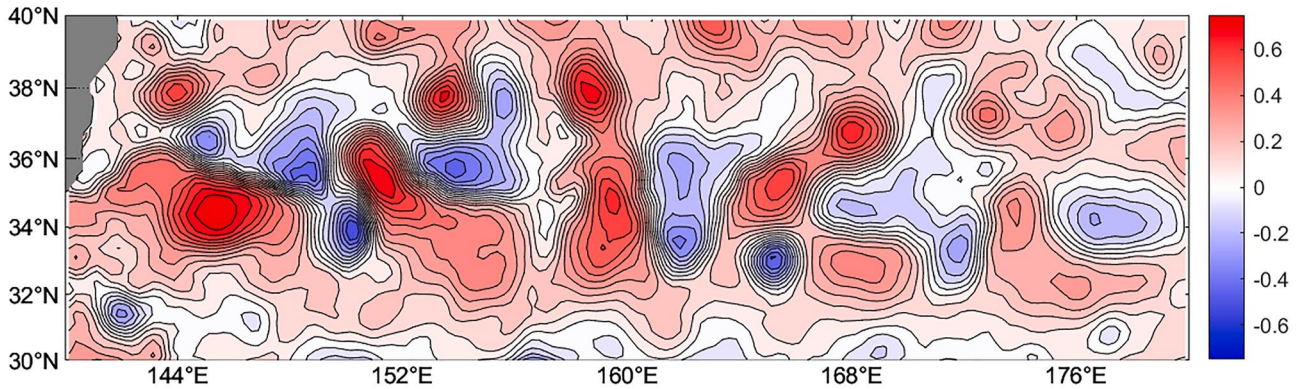
Figure 1. The sea surface height anomaly field (units: m) on 18 July 2018, which encompasses paired eddies, obtained from the Archiving, Validation, and Interpolating of Satellite Oceanographic altimeter data distributed by the Copernicus Marine and Environment Monitoring Service.

comparison with their work. Additionally, the conditional nonlinear optimal perturbation (CNOP) (Mu et al., 2003) approach is still employed.

The remainder of this paper is structured as below. In Section 2.1, the two-layer QG model is introduced. In Section 2.2, we briefly review a nonlinear approach named CNOP. In Section 3, we calculate CNOPs for paired mesoscale eddies related to SSHA forecasting and identify the sensitive areas accordingly. In Section 4, the effectiveness of target observation of paired eddies in enhancing SSHA forecasting skill is verified by conducting observing system simulation experiments. Section 5 interprets the reason behind the significant improvement in SSHA forecasts associated with targeted observations for paired mesoscale eddies. Finally, the summary and discussion are offered in Section 6.

2. Model and Method

2.1. The Two-Layer Quasigeostrophic Model

The doubly periodic (QG; Weiss & Grooms, 2017; Jiang et al., 2022) model with two equal layers is adopted. The model is constructed on the *f*-plane and is subject to a vertically sheared zonal flow with horizontally uniform and baroclinically unstable. By decomposing the instantaneous field into a mean field and a perturbation field, the governing equations for the evolution of perturbations derived from the two-layer QG model are expressed as follows:

$$\partial_t q_1 = -\mathbf{U}_1 \cdot \nabla q_1 - \partial_x q_1 - v_1 - \nu \nabla^8 q_1 \tag{1}$$

$$\partial_t q_2 = -\mathbf{U}_2 \cdot \nabla q_2 + \partial_x q_2 + v_2 - c_d \cdot \nabla \times (|U_2|U_2) - \nu \nabla^8 q_2 \tag{2}$$

$$q_1 = \nabla^2 \psi_1 + \frac{1}{2}(\psi_2 - \psi_1) \tag{3}$$

$$q_2 = \nabla^2 \psi_2 - \frac{1}{2}(\psi_2 - \psi_1) \tag{4}$$

where q_i and ψ_i represent the potential vorticity and streamfunction ($i = 1, 2$, representing the first and second layers of the model), $\mathbf{U}_i$ denotes the two-dimensional vector composed of zonal velocity $u_i = -\partial_y \psi_i$ and meridional velocity $v_i = \partial_x \psi_i$, $\nu (=5 \times 10^{-7})$ and $c_d (=0.1)$ are the hyperviscosity coefficient and standard quadratic drag coefficient, respectively. Equations 1–4 has been nondimensionalized, with the deformation radius and the imposed zonal velocity as length and velocity scales. The configuration of the model is as employed in the study conducted by Jiang et al. (2022). Particularly, the model domain is square with nondimensional width of 32π, nondimensional grid size of 0.39 (enabling that the deformation radius encompasses more than two grid points to meet the requirements for eddy-resolving computations), and nondimensional time step of 0.01. Then, the spatial grid size and the velocity are assigned dimensional values of 15 km and 0.01 m s^{-1}, respectively; this results in a

dimensional domain width of 3,840 km, a dimensional deformation radius of 38.2 km, and a dimensional time scale of about 42 days for this model. The numerical solutions of this model are computed by 256×256 nonzero Fourier modes and a fourth-order semi-implicit Runge-Kutta scheme.

2.2. Conditional Nonlinear Optimal Perturbation

To reveal the sensitive area associated with paired mesoscale eddies and fully take the nonlinearity of eddies into account, the (CNOP; Mu et al., 2003) approach is first adopted to investigate the most sensitive area of paired eddies associated with SSHA forecasts. The CNOP method has been applied to the studies of target observation in relation to Tropical Cyclones, El Nino-Southern Oscillation, Indian Ocean dipole, and Kuroshio large meander and the identification of their respective optimal observing locations according to the sensitivity of the most sensitive error revealed by the CNOP (Qin et al., 2013; Mu et al., 2017; Duan et al., 2018; Wang et al., 2013). Now, let's provide a brief introduction to the CNOP approach, specific details can be found in Mu et al. (2003) and Jiang et al. (2022).

The QG model can be abstracted as

$$X_t = M_t(X_0) \tag{5}$$

where X_t represents the state vector of the model at the prediction time t, which is obtained through "propagating" the initial state X_0 to the future time t using the nonlinear propagator M_t. Assuming that the initial condition X_0 is disturbed by x_0, then the solution is expressed as

$$X_t + x_t = M_t(X_0 + x_0) \tag{6}$$

where $x_t = M_t(X_0 + x_0) - M_t(X_0)$ indicates the nonlinear evolution of the initial perturbation x_0. To calculate the initial perturbation that leads to the most significant development at the prediction time within a given constraint radius δ, we define the nonlinear constraint optimization problem as Equation 7.

$$J(x_0^*) = \max_{x_0 \in C_\delta} J(x_0), \; J(x_0) = \|M_t(X_0 + x_0) - M_t(X_0)\|_A \tag{7}$$

C_δ restricts the range of the initial perturbations, $\| \cdot \|_A$ represents a norm which measures the evolution of perturbation at the prediction time with respect to reference state, J is the objective function. Obviously, the x_0^* exactly represents the CNOP focused in this paper, which denotes the initial perturbation that has the potential to cause the most significant forecast errors at the verification time t within the verification area, given the specific constraint radius δ.

In the QG model, the SSHA can be defined from the streamfunction of the first layer ψ_1. In view of our concerns here, the objection function can be rewritten as

$$J(\psi_{0\delta}^*) = \max_{\psi_{1,0}^* \in C_\delta} J(\psi_{1,0}^*), \; J(\psi_{1,0}^*) = \|M_t(\psi_{1,0} + \psi_{1,0}^*) - M_t(\psi_{1,0})\|_A \tag{8}$$

Then, L2 norm is chosen as $\| \cdot \|_A$ here. The scope of the initial perturbations is described as $C_\delta = \left\{ \psi_{1,0}^* \middle| \sqrt{\frac{1}{n} \sum_{i=1}^n (\psi_{1,0}^*)_i^2} \leq \beta \cdot (\psi_{1,0})_{STD} \right\}$, n denotes the number of grids perturbed, β denotes a preassigned positive number, $(\psi_{1,0})_{STD}$ represents the standard deviation of the $\psi_{1,0}$ (the initial filed of ψ_1 which perturbed by $\psi_{1,0}^*$ here) over the whole model scope. Note that β is set as 0.04 here according to practical observational errors of SSHA to guarantee the initial perturbations of SSHA at each grid point is constrained within the dimensional observational errors of 0.02–0.03 m.

After setting all the optimization problems, the objective function J in Equation 8 is calculated, and its maximum is obtained by applying the spectral projected gradient 2 (SPG2; Birgin et al., 2000) optimization algorithm. The SPG2 algorithm for calculating CNOPs requires the gradient information of the cost function with respect to initial perturbations, where the gradient was often calculated by integrating an adjoint model more efficiently. However, the QG model here does not have its adjoint ready, then we intend to calculate the gradient using

approach of numerical derivatives. Based on the automated and iterative forward integration of the QG model controlled by the SPG2, a given initial perturbation is optimized and updated according to the gradient till the convergence condition in the SPG2 is satisfied. The resulting initial perturbation is then regarded as the CNOP. For more details, please refer to Jiang et al. (2022).

3. The Most Sensitive Initial Error of Paired Mesoscale Eddies Associated With SSHA Forecasting

The CNOPs correspond to initial perturbations (or errors) that adhere to specific physical constraints and exhibit the most significant nonlinear evolution within the focused area (or verification area) at a specified prediction time (or verification time). The CNOPs act as the most sensitive initial perturbations in a nonlinear model, possessing a remarkable ability to pinpoint sensitive areas for target observation (Duan et al., 2023). The CNOP generally possesses areas of much large perturbation energies and the forecast accuracies are often much sensitive to the initial errors in these areas. Such areas could represent the sensitive areas for targeting observations. Now, we adopt this CNOP approach to explore the sensitive areas for targeting observations of paired mesoscale eddies, aiming to optimize initial field and ultimately enhance the forecast accuracy of SSHA.

To do so, we initially integrate the two-layer QG model, starting from an initial matrix composed of random numbers that follow a normal distribution $N(0,1)$ of (ψ_1, ψ_2), up to time T_0, so as to obtain a stable model field containing mesoscale eddies. Subsequently, with the streamfunction (ψ_1, ψ_2) at time T_0 as the initial value, we further integrate the model to time T_1 $(T_1 > T_0)$. The duration between T_0 and T_1 is 1 week (that is, 7 days, the same as that in Weiss and Grooms (2017) and Jiang et al. (2022)). Taking the time-dependent evolution of the SSHA over one week, specifically the 350th week here within the integration mentioned above, as a reference state for prediction, the CNOPs of the initial SSHA are calculated, in which the initial perturbation and its final state only pertain to the SSHA ψ_1 confined within a specific rectangle. This rectangle encompasses both the initial and final locations of two paired mesoscale eddies in spatial proximity (<200 km apart) (the eddies here are recognized by a simplified SSHA-based vortex identification algorithm; please see Appendix A in Jiang et al. (2022)).

Paired mesoscale eddies, as mentioned in the introduction, are generally configured including counter-rotating pairs and co-rotating pairs. Then, we conduct experiments respectively for these two configurations and compare their CNOPs. Specifically, 10 counter-rotating pairs and 10 co-rotating pairs are respectively selected. Then a total of 20 CNOPs are obtained with the respect to SSHA forecasting.

By observing the 10 CNOPs of counter-rotating/co-rotating pairs, it is found that similar features emerge within different counter-rotating cases/co-rotating cases, but distinctions are apparent between counter-rotating and co-rotating cases. That is, the counter-rotating eddies present the CNOPs mainly situated within the eddies, while the co-rotating eddies show the CNOPs located not only within the eddies but also between the two eddies (see Figure 2). More specifically, the former type of CNOP errors tend to locate the areas where eddies manifest clear high-to low-velocity gradients along their rotation, and they appear as a shear structure in SSHA; while the latter type of CNOPs, besides sharing the feature of the former CNOPs, further concentrate between the two eddies and obliquely tangential to their boundaries with a positive-negative SSHA shear structure. This finding suggests that the SSHA forecasting may be highly sensitive to not only the accuracy of initial eddy itself but also the initial field between the eddies in pairs, especially for the co-rotating eddies, which extends the results of Jiang et al. (2022) when they regarded the mesoscale eddy as an isolated body and did not consider the eddy-eddy interaction.

From the above, it is known that the areas located in the CNOP patterns and bearing large perturbation energies could represent sensitive areas for targeting observation. Then these possible sensitivities suggest that, apart from the sensitive areas on the eddies themselves, the areas situated between two eddies in pairs and obliquely tangential to their boundaries may also be the sensitive areas, especially when two co-rotating eddies are investigated. Next, we perform numerical experiments to examine the feasibility of the sensitive areas of paired eddies.

4. Observing System Simulation Experiments to Examine the Feasibility of the Sensitive Areas for Paired Eddies

As described in the introduction, the purpose for targeting observations is to provide the most useful additional observations, so as to provide a more precise initial field for the numerical model, thus much effectively improving the concerned forecast skill. The "target observation" mainly serves the demand of forecasts on
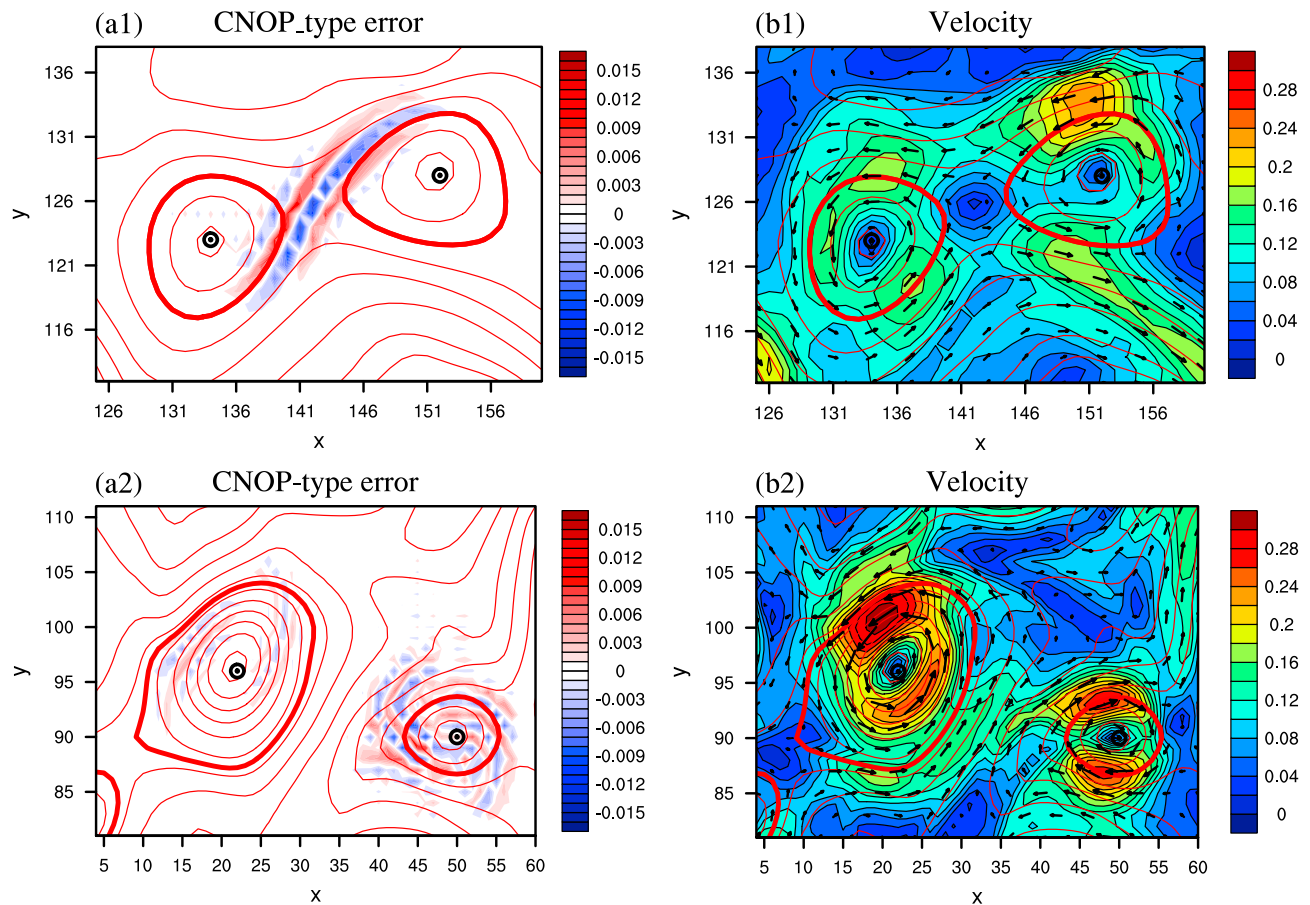
Figure 2. The left panels depict the conditional nonlinear optimal perturbations (CNOPs) associated with 7-day sea surface height anomaly (SSHA) forecast (a; shaded) (units: m); the right panels illustrate the initial velocity field of paired eddies with respect to the CNOPs shown in the left panels (b; shaded) (units: m s^{-1}). (1) and (2) denote the case involving paired co-rotating eddies and paired counter-rotating eddies respectively. The black "⊙" marks the centers of the mesoscale eddies at initial time, the red contours depicts the SSHA field, bold contours denote the edges of eddies, the black arrows indicate the velocity vectors.

observations (Snyder, 1996), which is different from traditional observation strategies, that is, to recognize the phenomenon and understand its mechanism. Notably, a series of encouraging results have been achieved in theoretical research and related field experiments of target observations for high-impact weather and climate event forecasting. For example, the Observing Systems Research and Predictability Experiment and the program of Dropwindsonde Observation for Typhoon Surveillance near the Taiwan Region both used the target observation strategy to reveal the important role of the additional observations in sensitive areas in improving the forecasting ability of typhoon (Wu et al., 2007, 2009).

In this section, we confirm the rationality of the above possible sensitive areas for targeting observations of paired mesoscale eddies recognized by the CNOPs through conducting observing system simulation experiments (OSSEs) along with the thinking of predictions. We first assess the sensitive areas of counter-rotating pairs which are only located within the eddies themselves and present significant high-to low-velocity gradients in flow fields. The corresponding OSSEs confirm the rationality of these sensitive areas and provide very similar results to those of Jiang et al. (2022), which established the validity of the sensitive areas precisely located on mesoscale eddies and also characterized by clear high-to low-velocity gradients through treating eddies as isolated bodies. Then, we refrain from providing further redundant descriptions here. Now we focus on investigating the rationality of the sensitive areas for co-rotating pairs, which are situated not only in areas exhibiting clear high-to low-velocity gradients on the eddies themselves but also in areas between two eddies in pairs and obliquely tangential to their boundaries.
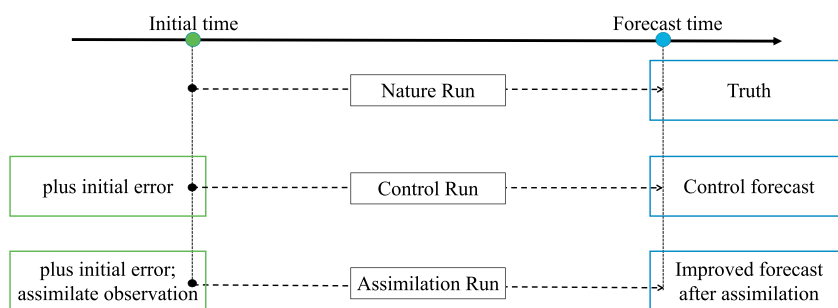
Figure 3. The schematic diagram of observing system simulation experiment process.

In the OSSEs, the reference state spanning from T_0 to T_1 is chosen to represent the "true" state, hereafter referred to as the "Nature Run," and the synthetic observations are generated by introducing errors into the Natural Run at given observation sites. Subsequently, we superimpose white noise with a larger amplitude on the Nature Run at time T_0 and smooth this field with white errors by Lanczos filtering algorithm. Using the smoothed field as initial condition, the model is integrated until time T_1 to create the "Control Run," which essentially serves as a control forecast of the Nature Run. Then, we assimilate synthetic observations into the initial field of the Control Run, resulting in an updated initial field. Using the revised initial field, we once again integrate the model to generate a new SSHA forecast. For simplicity, we will call this new forecast the "Assimilation Run" (see Figure 3).

Note that various control forecasts will yield different forecast errors, primarily originating from distinct initial errors, which refer to the disparities between the initial fields of Natural Run and Control Runs. Certain initial errors may result in minimal forecast errors, while others can lead to significantly large forecast errors. When initial errors result in negligible forecast errors, the forecast results are already satisfactory. In such instances, even if we assimilate targeted observations into the model, the improvement in forecasts is often imperceptible. However, in cases where initial errors result in large forecast errors, the assimilation of targeted observations becomes imperative, which will help effectively optimize initial field and lead to a significant enhancement in prediction skills. Therefore, to conduct a more realistic and reasonable evaluation of targeted observations, we intentionally select the Control Runs with significant forecast errors for assimilation experiments. Concretely, we generate 100 Control Runs and get 100 initial errors by taking the difference between Control Runs and Nature Runs at time T_0. All initial errors are scaled to the same amplitude through $X_i' = \lambda_i X_i$, where X_i and X_i' ($i = 1, 2\ldots, 100$) respectively represent the initial errors of the Control Run and their scaled counterparts; λ_i is a scaling factor, making X_i' satisfy $\sqrt{\sum_{j=1}^{N} (X_{i,j}')^2 / N} = \alpha \delta_0$, where j is a grid point, N is the total number of grid points within the rectangular area where two initially interacting eddies are located, as well as their positions after 1 week of evolution, α denote a given positive value constraining the magnitude of the initial errors of Control Runs, δ_0 represents the standard deviation of the initial values in the reference states of SSHA. Considering the magnitude of initial errors in practice, We set α to 0.2 here (sensitivity experiments confirmed that variations within a certain range of this value have a negligible impact on the final experimental results). Then, we examine the forecast errors resulting from all the scaled initial errors and select the top 20 initial errors that lead to larger forecast errors for conducting the OSSEs.

For the 10 co-rotating eddy cases, whose sensitive areas are situated not only within the eddies but also between the two eddies and obliquely tangential to their boundaries for the SSHA forecasting over the regions covered by the rectangles encompassing both the initial and final locations of two paired mesoscale eddies (i.e., the validation region; see the description for target observation in the introduction), we adopt the above designment to conduct OSSEs and show the rationality of the sensitive areas. Similar results are obtained in different cases, and we will take the vortex in Figure 2a1 as an example to elucidate in detail. Specifically, we first extract 11 sub-regions within the region where initial perturbations are superimposed and the CNOP is calculated (this region is also the validation region for target observation). These regions have the same size covering 25 grid points, which are respectively denoted as R1 to R11 (see Figure 4). Notably, the region R5 is precisely situated between the two eddies in the co-rotating pair and covers the possible sensitive area tangential to the eddy boundaries; while the regions R10 and R11 cover precisely the possible sensitive areas located on mesoscale eddies. The remaining
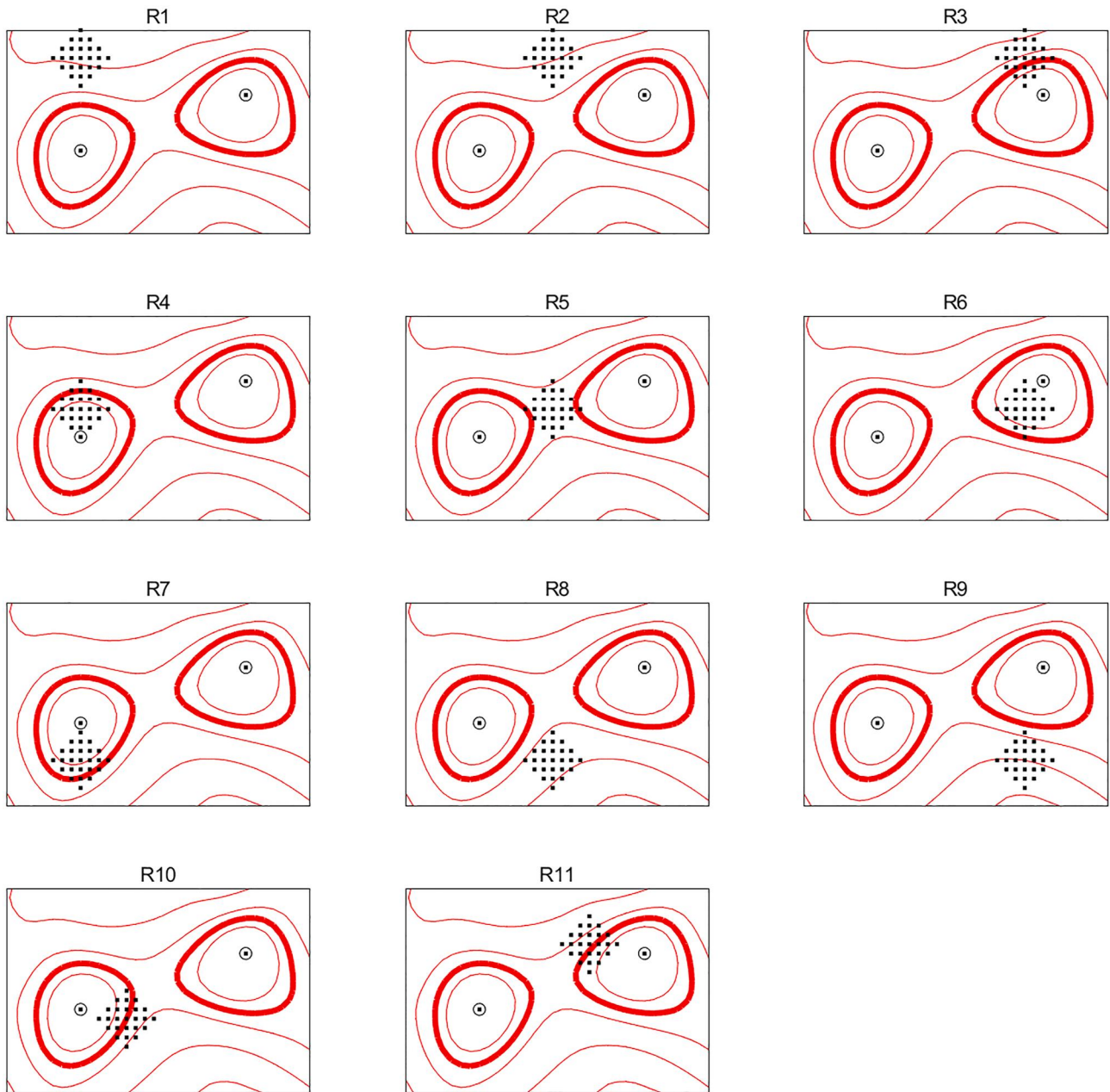
Figure 4. R1 to R11 represent 11 local regions that are uniformly extracted within the perturbation region for the specific case shown in Figure 2a1. In each region, 25 connected grid points marked with black points are selected. The black "⊙" represent the centers of the initial eddies.

selected sub-regions are almost ergodic in the rest of the validation region. Subsequently, for each of the sub-regions, we randomly deploy 20 sets of 2-point observations to generate various assimilation strategies. As an example, Figure 5 provides the assimilation strategies (G1-G20) randomly generated for the R5 region. Our intention is to demonstrate the substantial impact of assimilating targeted observations in the sensitive areas for the co-rotating eddies. Optimal interpolation is employed to assimilate observations here (please see Appendix D in Jiang et al. (2022)). The benefit, which indicates the improvement in SSHA forecasting obtained through assimilation, is quantified by the following Equation 9.

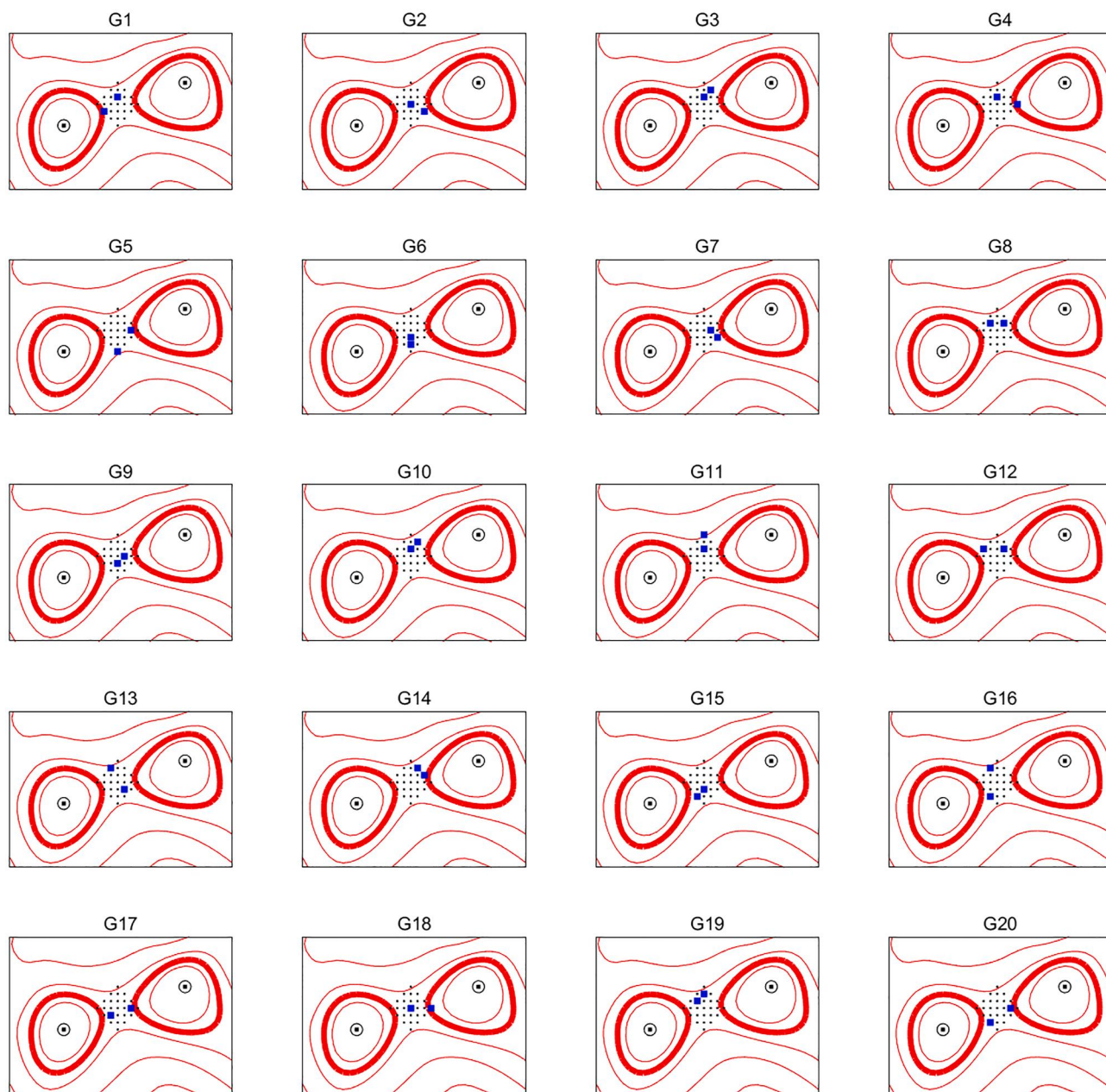$$b = \frac{dF_1 - dF_2}{dF_1} \times 100\%, \tag{9}$$

Figure 5. G1-G20 represent 20 assimilation strategies of R5 region. In these strategies, two-grid observations are randomly deployed within the R5 region situated between two co-rotating eddies, which are marked by bold blue dots.

where dF_1 and dF_2 represent the forecast errors of the Control Run and the Assimilation Run, respectively, relative to the Nature Run.

Utilizing these different assimilation strategies, the model is integrated, and the benefits (denoted as "b") from assimilating targeted observations are calculated. Similar results are obtained from different co-rotating eddies and then we describe the results using the case shown in Figure 2. As depicted in Figure 6, both median and mean values clearly indicate that the benefit b, indicating the improvement of SSHA forecasting skill resulting from assimilating observations, in the R5 region is comparable to that in the R10-R11 regions, and notably higher than that in other nonsensitive regions. From these experiments, we confirmed that the preferential deployment of additional observations in the sensitive area (i.e., R5) situated between two co-rotating eddies and obliquely tangential to their boundaries is indeed a valid strategy for improving the forecast accuracy of SSHA. Importantly,
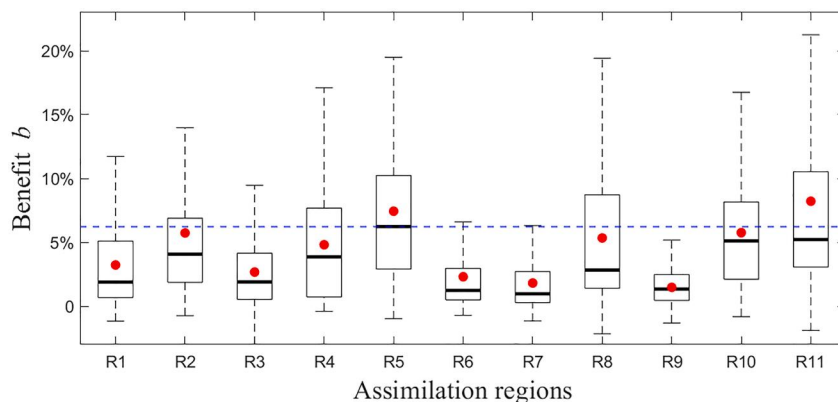
Figure 6. Boxplot of the benefits *b* resulting from assimilating various two-grid observations in regions R1 to R11 with respect to 20 Control Runs with larger forecast errors. The red dots and bold black lines represent the mean and median, respectively.

its effectiveness is comparable to that in the sensitive areas (i.e., R10 and R11) characterized by clear high-to-low-velocity gradients within eddies. Additionally, similar results were obtained when deploying 3-point or 4-point observations in 20 different assimilation strategies, reaffirming the consistency of these findings.

Furthermore, upon conducting a more in-depth analysis of the improvement effects of different assimilation strategies (i.e., the 20 sets of 2-point observations randomly deployed in corresponding sub-regions) on predictions, it is evident that the structure of CNOPs offers valuable guidance for determining the deployment with specific arrays of target observations. Basically, the benefits of assimilation become evident only when observations are strategically placed in sensitive areas, whether they are situated within or between the two co-rotating eddies, with an array crosscutting the shear structure of CNOPs. Specifically, for the sensitive areas within eddies, such as the R10 and R11 regions, this array is displayed along the radial direction of eddy, which aligns with Jiang et al. (2022). Their work has thoroughly described this aspect and provided a reasonable explanation from the perspective of barotropic instability, so we will refrain from reiterating or elaborating on it here. While for the sensitive areas situated between the two eddies, such as the R5 region, this array manifests perpendicular to the line connecting the centers of the two interacting eddies, as illustrated in Figures 5 and 7. This has not been found in previous works. Such observational arrays effectively cut off the possible shear structure of the initial errors similar to the CNOPs and are beneficial for capturing the spatial characteristic of the optimally growing perturbations occurring between two co-rotating eddies and obliquely tangential to their boundaries. By assimilating these observations, we are able to effectively mitigate the influence of CNOP on SSHA forecasting, leading to significant improvements in predictive accuracy. However, there is currently no exact theoretical mechanism to explain why target observation in the sensitive area situated between two co-rotating eddies, especially with a specific observation array oriented perpendicular to the line connecting the centers of the two interacting eddies

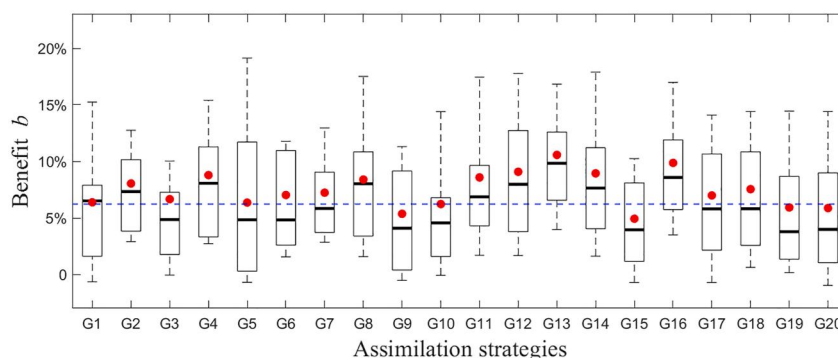**Figure 7.** Boxplot of the benefits *b* obtained from assimilating various two-grid observations in G1-G20 with respect to 20 Control Runs with larger forecast errors. The red dots and bold black lines represent the mean and median, respectively.

which effectively intersect the possible shear structure of the initial errors similar to the CNOPs, can significantly improve forecasting skills. An explanation for this phenomenon is warranted and we will discuss it in the next section.

5. Interpretation

Now, we will elucidate why target observations deployed in the sensitive area situated between two co-rotating eddies with the array oriented perpendicular to the line connecting the centers of the two co-rotating eddies can lead to a more significant improvement in SSHA forecast skill. Given that this particular configuration of target observation is determined by the characteristics of CNOPs, the key inquiry revolves around understanding why CNOPs located in the region between two co-rotating eddies exhibit such characteristics and can experience significant growth, ultimately exerting a profound influence on the forecast results. In order to clarify this issue, the eddy-energies analysis is utilized below (Tsujino et al., 2006).

Typically, the decomposition of an instantaneous flow field into mean flow and eddy fluctuation is involved in the calculation of eddy energies. The mean flow is usually obtained by temporally averaging the instantaneous field, while the eddy fluctuation is represented as the difference between the instantaneous field and the mean field. In the case of horizontal mean flow, it is generally believed that the development of eddy fluctuation is primarily driven by the barotropic instability of the mean flow, which facilitates the transfer of energy, particularly kinetic energy, to sustain the growth of eddy fluctuations. The barotropic conversion rate (BT) is commonly used to quantify the transfer of kinetic energy from the mean flow to the eddy fluctuation induced by barotropic instability, and it can be derived from the tendency equation of eddy kinetic energy (EKE) under the QG assumption, as expressed by the following Equation 10.

$$\frac{\partial(\text{EKE})}{\partial t} = -\rho_0\left(u'u'\frac{\partial\overline{u}}{\partial x} + u'v'\left(\frac{\partial\overline{u}}{\partial y} + \frac{\partial\overline{v}}{\partial x}\right) + v'v'\frac{\partial\overline{v}}{\partial y}\right)$$
$$- \overline{\boldsymbol{u}}\cdot\nabla(\text{EKE}) - \boldsymbol{u'}\cdot\nabla(\text{EKE}) - \boldsymbol{u_a'}\cdot\nabla P' - W'\frac{\partial P'}{\partial Z} - g\delta\rho'w' \tag{10}$$

The terms on the right-hand side can be understood as horizontal momentum fluxes that are oriented down the mean momentum gradient, the mean advection of EKE, the eddy advection of EKE, horizontal and vertical eddy pressure work by the ageostrophic flow, and vertical buoyancy fluxes, respectively (see Tsujino et al. (2006) for more details). The first term is interpreted as the BT from mean kinetic energy to eddy kinetic energy. That is

$$\text{BT} = -\rho_0\left(u'u'\frac{\partial\overline{u}}{\partial x} + u'v'\left(\frac{\partial\overline{u}}{\partial y} + \frac{\partial\overline{v}}{\partial x}\right) + v'v'\frac{\partial\overline{v}}{\partial y}\right). \tag{11}$$

where $\overline{u}$ and $\overline{v}$ are zonal and meridional velocities of the mean flow, u' and v' are the corresponding velocities of the eddy fluctuation field, respectively. Obviously, when BT is positive, the EKE is transferred from mean flow to eddy fluctuation.

It's important to note that different definitions of mean flow or eddy fluctuations may be applicable to specific physical problems of interest. Even so, the BT can still serve as an indicator of barotropic instability (Fujii et al., 2008). With regard to the specific issue concerned here, the reference state for prediction, which is confined to the regions covered by rectangles encompassing both the initial and final locations of two paired mesoscale eddies, is considered as mean flow, while the CNOPs are viewed as eddy fluctuations. Then, the BT related to the CNOPs is calculated using Equation 11, and it is found that the positive BT consistently appears in the area with significant CNOPs (see Figure 8). Specifically, in addition to the locations where eddies exhibit clear high-to low-velocity gradients, positive BT also appears in the area between two co-rotating eddies and obliquely tangential to their boundaries. Hence, it can be concluded that the initial errors between two co-rotating eddies are also indeed more likely to extract energy from the reference state and experience significant growth, which consequently have a crucial impact on the prediction of SSHA.

Then, apart from the areas within eddies characterized by clear high-to low-velocity gradients, which has been explained in the work of Jiang et al. (2022), why does the positive BT also exist between two co-rotating eddies in pairs and obliquely tangential to their boundaries? We notice that within the region between two co-rotating
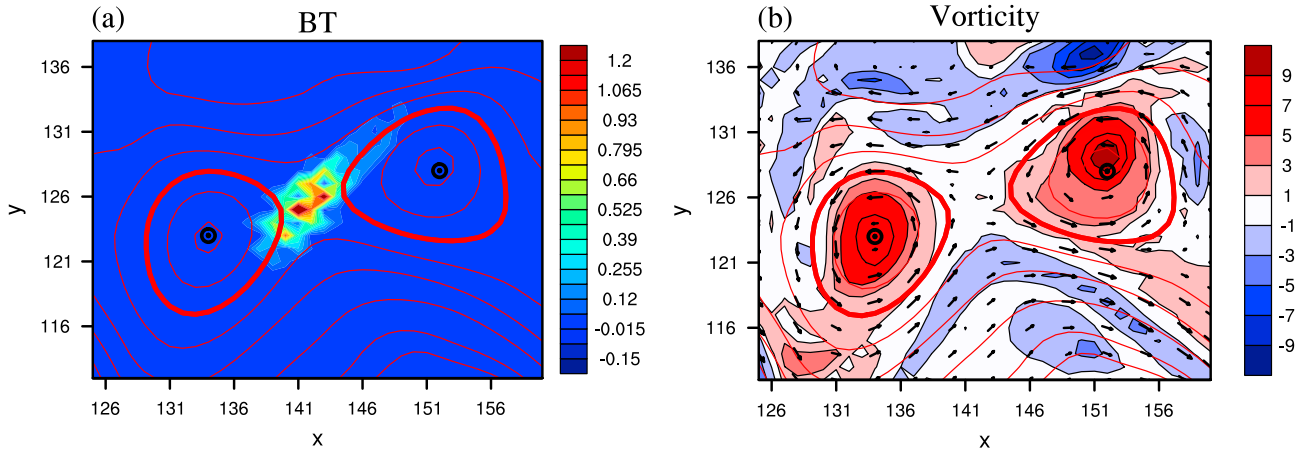
Figure 8. (a) The distribution of the BT (units: $10^{-7}\text{m}^2\text{s}^{-3}$) associated with the reference state and its corresponding conditional nonlinear optimal perturbations in Figure 2a1; (b) the corresponding vorticity (shaded; 10^{-6}s^{-1}) of initial field.

cyclonic or anticyclonic eddies, there consistently exists a prominent maximum or minimum vorticity. That reminds us of the Rayleigh criterion for barotropic instability, which was originally defined by Rayleigh (1880). According to this criterion, barotropic instability occurs only when extreme vorticity is present within a specific region (for the detailed derivation of this criterion, please see Rayleigh (1880); Emanuel (2009)). Consequently, in the region positioned between two co-rotating eddies, in contrast to the scenario involving two counter-rotating eddies, initial errors have the capacity to obtain energy from the reference field through barotropic instability. This leads to the rapid amplification of initial errors and ultimately leads to significant prediction errors (Figure 9).

After elucidating the reason behind the presence of significant CNOP values within the area between two co-rotating eddies, the next step is to provide a comprehensive explanation of the shear structure that presents a positive-negative contrast in SSHA of the calculated CNOPs here. To address this issue, Equation 11, which is derived based on the Cartesian rectangular coordinate system, is further simplified and analyzed. In essence, the Cartesian rectangular coordinate system is composed of two perpendicular coordinate axes intersecting at the origin. Then, we can establish the coordinate axes of the Cartesian coordinate system in a flexible manner based on the concerned problems.

As is well known, barotropic instability arises from the horizontal velocity shear in the mean flow. Assuming that there is a mean flow with horizontal shear, as depicted in Figure 10, we can establish the X-axis along the direction of fluid shear. In this case, there exists $\overline{u} \neq 0, \frac{\partial \overline{u}}{\partial x} = 0, \overline{v} = 0$, and Equation 11 can be further simplified accordingly:

$$\text{BT} = -\rho_0 u'v' \frac{\partial \overline{u}}{\partial y} \qquad (12)$$

Further, we establish the Y-axis according to the basis $\frac{\partial \overline{u}}{\partial y} > 0$. Density ρ_0 is always a positive value. Under this circumstance, BT > 0 can be guaranteed as long as $u'v' < 0$ is satisfied. It's evident that when the disturbance velocities $\boldsymbol{u'}(u',v')$ are either perpendicular or parallel to the coordinate axes, indicating $u' = 0\ or\ v' = 0$, there will be $u'v' = 0$, which does not meet the requirement $u'v' < 0$. Therefore, there must be an angle between the disturbance velocities and the mean shear flow, as depicted in Figure 10 (we established the disturbance velocity in the first and second quadrants). Through further analysis, we found that only when there exists an obtuse angle θ_2 from the positive direction of the X-axis to the scalar direction of the disturbance velocity in counterclockwise rotation, $u'v' < 0$ can be guaranteed. Correspondingly, BT > 0 at that time. Therefore, only this type of disturbance flow has the potential to obtain energy from reference state and cause significant prediction errors. The θ_2 exactly suggests the approximate direction followed by the shear structure of CNOPs in the area between two co-rotating eddies.
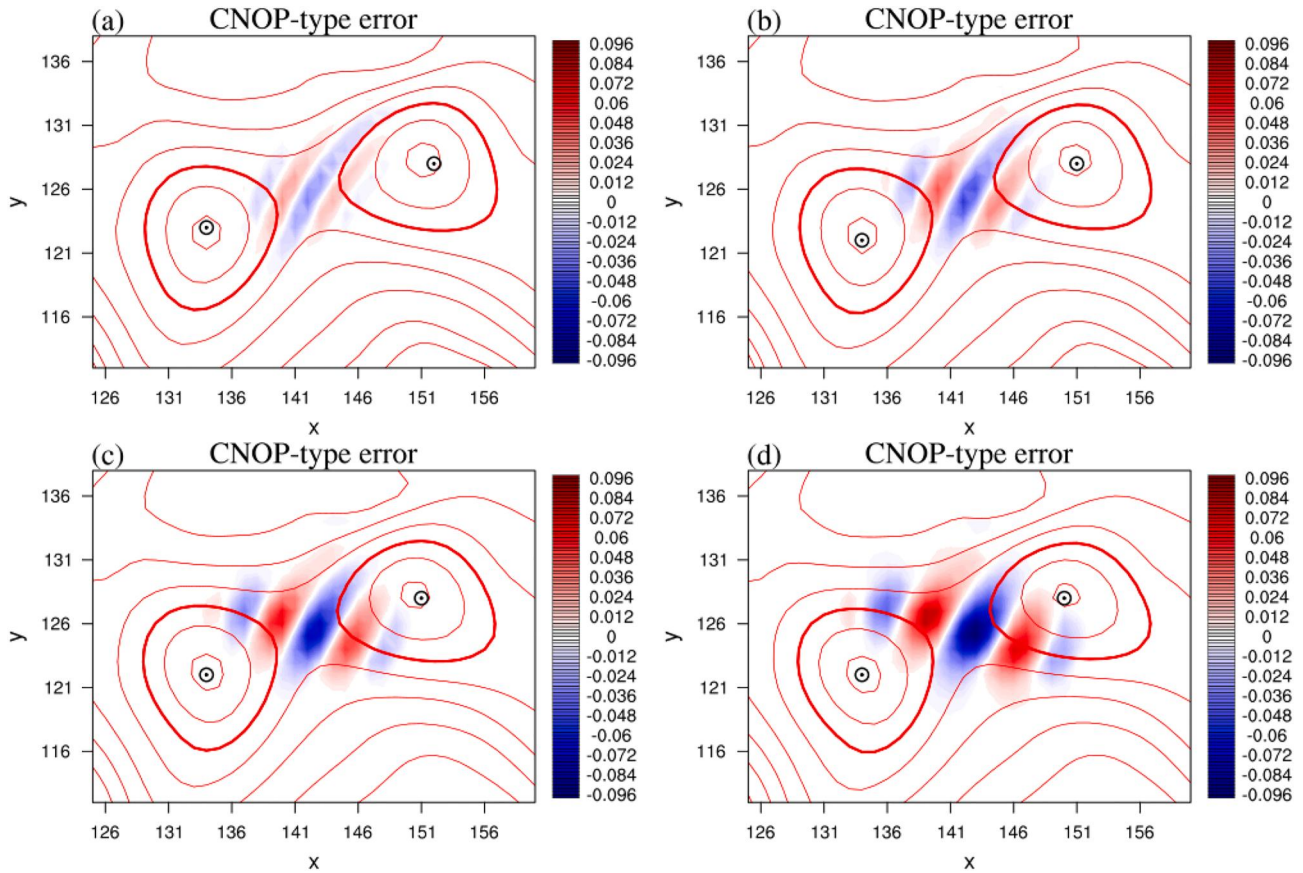
Figure 9. The conditional nonlinear optimal perturbations and their evolution (shaded) concerning the initial paired eddies in Figure 2a1 are plotted in (a) for the time $\frac{1}{4}(T_1 - T_0)$, (b) for the time $\frac{1}{2}(T_1 - T_0)$, (c) for the time $\frac{3}{4}(T_1 - T_0)$, and (d) for the time T_1, where $[T_0, T_1]$ corresponds to the optimization period in Section 3. The red contours draw the outline of the sea surface height anomaly fields, the bold closed contours represent the edge of the eddies. The black "⊙" marks the centers of the mesoscale eddies at corresponding time.

Now, we have introduced the angle θ into the coordinate system. This brings us neatly to further describe the $u'v'$ in a polar coordinate system, which is constructed based on the Cartesian coordinate system established above. Wherein, the polar coordinate system takes the origin of the Cartesian coordinate system as the pole O, the X axis as the polar axis, and the angle is considered positive when measured in the counterclockwise direction. Any point P on the plane can be positioned using two fundamental components: the length of the line segment OP (called the polar diameter r) and the angle from OX to OP (called the polar angle θ). This ordered number pair P (r, θ) is referred to as the polar coordinate of point P. Then, $u'v'$ can be expressed as
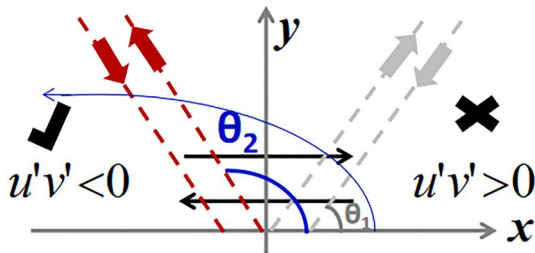

Figure 10. Sketch map for theoretically interpreting the inclined direction of the shear structure of conditional nonlinear optimal perturbations between two co-rotating eddies. The solid black lines with arrows represent the assumed horizontal velocity shear. The solid gray lines with arrows represent the Cartesian coordinate axes x and y established based on the velocity shear, with the x-axis also corresponding to the polar axis in the polar coordinate system. The thin blue line with an arrow indicates the positive direction of an angle in the polar coordinate system. The bold gray/red arrows represent vector velocities which satisfies $u'v' > 0/u'v' < 0$, with the θ_1/θ_2 corresponds to the angle in the polar coordinate system.

$$
\begin{aligned}
u'v' &= -\frac{\partial \psi'}{\partial y} \cdot \frac{\partial \psi'}{\partial x} \\
&= \underbrace{-\frac{\sin 2\theta}{2}\left(\frac{\partial \psi'}{\partial r}\right)^2}_{(I)} + \underbrace{\frac{\sin 2\theta}{2r^2}\left(\frac{\partial \psi'}{\partial \theta}\right)^2}_{(II)} - \underbrace{\frac{\cos 2\theta}{r}\left(\frac{\partial \psi'}{\partial r}\frac{\partial \psi'}{\partial \theta}\right)}_{(III)}
\end{aligned}
\tag{13}
$$

According to the above analysis, in order to ensure a positive BT, it is necessary to have $90° < \theta < 180°$, which leads to the condition $u'v' < 0$. Correspondingly, when $90° < \theta < 180°$, there exists $\sin 2\theta < 0$, resulting in the term (I) > 0, the term (II) < 0, and the term (III) > 0 or < 0. Since the term (I) and the term (II) are ensured to be positive and negative respectively, to
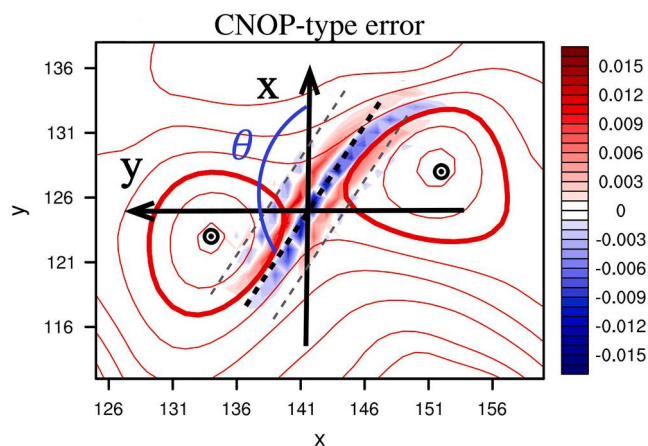
Figure 11. Sketch map for theoretically interpreting the shear structure of conditional nonlinear optimal perturbations between two co-rotating eddies. The solid black lines with arrows represent the Cartesian coordinate axes x and y established based on the velocity shear, with the *x*-axis also corresponding to the polar axis in the polar coordinate system. The θ corresponds to the angle in the polar coordinate system. The dotted lines indicate the polar diameter.

maximize the positive BT, it is desirable for the absolute value of the term (I) to be as small as possible, ideally equal to 0, and the absolute value of the term (II) to be as large as possible. Since both term (I) and term (II) contain the factor $sin2\theta$, we will temporarily set it aside for now. Then, the $\frac{\partial \psi'}{\partial r}$ in term (I), which means the shear of ψ' along the polar diameter direction, is preferably as small as possible, even equal to 0, which then correspondingly results in term (III) being equal to 0. On the other hand, in term (II), the $\frac{\partial \psi'}{\partial \theta}$ is desired to be as large as possible, indicating that the ψ' is better to show the strongest shear along the polar angle direction. Besides, in order to obtain the maximum positive BT, the maximum absolute value of $sin2\theta$ also needs to be considered in term (II), which is achieved when $\theta = 135^{\circ}$.

Up to now, we have gained a clear understanding of the structural features of our calculated CNOPs located between two co-rotating eddies and obliquely tangential to their boundaries. That is, as in Figure 11, the shear structure in positive-negative contrast, as observed in CNOPs, aligns with the expected strongest shear structure along the polar angle direction; meanwhile, the shear structure of the calculated CNOPs precisely presented $\theta = 135^{\circ}$ in our build flexible coordinate. Our calculated CNOPs that satisfied these two elements would induce the largest positive BT between two co-rotating eddies, subsequently exerting the most significant influence on forecast errors.

To sum up, through the theoretical analysis presented above, we reasonably explained the sensitive area and the shear structure of CNOP between two co-rotating eddies from the perspective of barotropic instability. Specifically, when initial errors exhibit a pronounced shear structure with a positive-negative contrast in SSHA aligned in a fixed direction, similar to the CNOPs computed in this study, and are superimposed within the area situated between two co-rotating eddies where extreme vorticity values exist in the reference states, it results in the generation of a larger positive BT. Consequently, most of the energy is transferred from the reference state to the errors, facilitating their optimal growth. Therefore, by prioritizing additional observations in the area between two co-rotating eddies with an array displayed perpendicular to the line connecting the centers of the two interacting eddies, the impact of this initial error on the forecast can be minimized, resulting in a more effective improvement in SSHA prediction skills.

6. Summary and Discussion

Given that mesoscale eddies in the world's oceans typically manifest in pairs, this study presents the first investigation into the impact of paired mesoscale eddies on the sensitivity related to SSHA forecasting by unilizing the CNOP approach in a two-layer QG model. This research extends Jiang et al. (2022), where they treated mesoscale eddies as isolated bodies to identify their sensitive areas. Firstly, the most sensitive initial errors of paired mesoscale eddies for SSHA forecasts are calculated. Specifically, for counter-rotating eddies, the CNOPs primarily manifest within the eddies themselves, particularly in areas featuring noticeable high-to low-velocity gradients within the eddies, and they are characterized by a shear structure in SSHA. While for co-rotating eddies, besides sharing the feature of the CNOPs of counter-rotating pairs, their CNOPs further concentrate between the two eddies and are obliquely tangential to their boundaries with a positive and negative shear structure. These findings indicate that the SSHA forecasting is highly sensitive not only to the accuracy of initial eddies themselves but also to the field situated between two paired eddies, especially for the co-rotating eddies. Correspondingly, it is suggested that, apart from the sensitive areas on the eddies themselves, the areas situated between two eddies and obliquely tangential to their boundaries could also be sensitive areas, especially when two co-rotating eddies are investigated.

Next, we conduct OSSEs to examine whether targeted observations in the sensitive areas determined by CNOPs can indeed improve SSHA forecasts and to evaluate the practicality of utilizing these sensitive areas for field observations. For each case consisting of two counter rotating/co-rotating eddies, we tried multiple observation arrays of randomly distributed 2 grids in either the sensitive or nonsensitive areas. These observations were

assimilated to evaluate the enhancement of SSHA forecasting accuracy and to propose a more efficient observation array for further improving SSHA forecasts. These results demonstrate that in cases of counter-rotating mesoscale eddies, the sensitive areas located precisely on eddies themselves are effective in SSHA prediction, which aligns with Jiang et al. (2022), where mesoscale eddies were considered as isolated bodies. For co-rotating eddies, it is crucial to highlight that, apart from target observation with a specific array in sensitive areas within eddies, prioritizing the implementation of additional observations in the sensitive areas between two co-rotating eddies, particularly with an array displayed perpendicular to the line connecting the centers of the two interacting eddies, can also effectively improve SSHA prediction skills.

Finally, we pay further attention to delving into why the target observation with a specific array deployed in sensitive areas, especially in the area between two co-rotating eddies, results in a greater improvement in SSHA forecast skill from the perspective of barotropic instability. The key lies in positive BT, which ensures that the initial errors get energy from the reference state and grow. Theoretical formula derivation indicates that when initial errors exhibit a pronounced shear structure with a positive-negative contrast in SSHA aligned in a fixed direction, similar to the CNOPs calculated in this study, and are superimposed on the area situated between two co-rotating eddies where extreme vorticity values exist in the reference states, it results in the generation of a positive BT. Consequently, most of the energy can be transferred from the reference states to initial errors, facilitating their optimal growth. Therefore, by prioritizing additional observations in the area between two co-rotating eddies with an array displayed perpendicular to the line connecting the centers of the two interacting eddies, the impact of initial errors, especially those growing rapidly during the optimization time (such as CNOPs), on the forecast can be minimized, resulting in a more effective improvement in SSHA prediction skills.

This research examines the accuracy of paired mesoscale eddies in relation to SSHA forecasting and holds the potential to make a substantial contribution toward the initialization of paired mesoscale eddies, consequently enhancing the precision of SSHA forecasts. We need to note that, in order to facilitate a comparison between the present study and Jiang et al. (2022), this study is limited to being conducted in a two-layer QG model, especially with a focus on the surface flow associated with eddy interaction. The CNOPs calculated in this study involve horizontal velocity shear of the background field, a characteristic typically associated with barotropic instability rather than baroclinic instability in the context of horizontal mean flow. A rational explanation for the position and structural characteristics of CNOPs between two co-rotating eddies is then provided from the perspective of barotropic instability. However, in practice, it is essential to recognize that mesoscale eddies usually have a three-dimensional structure (Zhang et al., 2019), implying the coexistence of baroclinic and barotropic instability. This coexistence may significantly impact the interaction between paired eddies. Hence, employing a more realistic model that includes pronounced baroclinic instability to investigate the impact of accurately representing paired mesoscale eddies on SSHA forecasts, and potentially other three-dimensional oceanic variables like temperature and salinity fields, becomes advantageous, especially considering the challenges of conducting observations below the sea surface. Additionally, the specific sensitivity of the sensitive areas between eddies may be influenced by factors such as the distance between eddies and the strength of the eddies. Further exploration of this issue also calls for more practical models, enhancing the applicability of guidance for target observations in field campaigns. It is essential to acknowledge the significant computational complexity involved in calculating CNOPs in more realistic weather models, but some intelligent algorithms, such as Particle swarm optimization, genetic algorithm, etc., offer promising solutions for high-dimensional optimization problems. These algorithms operate without the need for gradient calculations, making them potentially applicable to models of varying complexities. Thus, it is anticipated that these algorithms can be leveraged to compute CNOPs for more realistic models, paving the way for further exploration of paired eddies sensitivity in future studies. Furthermore, recent works have noted the significance of filamentary structures at the periphery of eddies in material transport (Liu & Abernathey, 2023; Liu et al., 2019). The findings of this study may hold important value for predicting material transport caused by eddies, presenting an interesting avenue for further research.

Data Availability Statement

Satellite altimetry data were sourced from the CMEMS website (https://marine.copernicus.eu). All scripts employed for data analysis and figure generation were developed using NCL (https://www.ncl.ucar.edu) and MATLAB (https://www.mathworks.com/products/matlab.html).

References

Agarwal, N., Sharma, R., & Kumar, R. (2022). Impact of along-track altimeter sea surface height anomaly assimilation on surface and sub-surface currents in the Bay of Bengal. *Ocean Modelling*, *169*(9), 101931. https://doi.org/10.1016/j.ocemod.2021.101931

Babiano, A., Boffetta, G., Provenzale, A., & Vulpiani, A. (1994). Chaotic advection in point vortex models and two-dimensional turbulence. *Physics of Fluids*, *6*(7), 2465–2474. https://doi.org/10.1063/1.868194

Birgin, E. G., Martínez, J. M., & Raydan, M. (2000). Nonmonotone spectral projected gradient methods on convex sets. *SIAM Journal on Optimization*, *10*(4), 1196–1211. https://doi.org/10.1137/S1052623497330963

Cheng, Y., Ho, C., Zheng, Q., & K, N. (2014). Statistical characteristics of mesoscale eddies in the North Pacific derived from satellite Altimetry. *Remote Sensing*, *26*(6), 5164–5183. https://doi.org/10.3390/rs6065164

Duan, W., Li, X., & Tian, B. (2018). Towards optimal observational array for dealing with challenges of El Nino-Southern Oscillation predictions due to diversities of El Nino. *Climate Dynamics*, *51*(9–10), 3351–3368. https://doi.org/10.1007/s00382-018-4082-x

Duan, W., Yang, L., Mu, M., Wang, B., Shen, X., Meng, Z., & Ding, R. (2023). Recent advances in China on the predictability of weather and climate. *Advances in Atmospheric Sciences*, *40*(8), 1521–1547. https://doi.org/10.1007/s00376-023-2334-0

Durán-Campos, E., Monreal-Gómez, M., Salas de Leon, D., & Coria-Monter, E. (2019). Impact of a dipole on the phytoplankton community in a semi-enclosed basin of the southern Gulf of California, Mexico. *Oceanologia*, *61*(3), 331–340. https://doi.org/10.1016/j.oceano.2019.01.004

Emanuel, K. (2009). *Quasi-balanced circulations in oceans and atmospheres—Barotropic instability*. Department of Earth, Atmospheric and Planetary Sciences, Massachusetts Institute of Technology.

Fedorov, A., & Belonenko, T. (2020). Interaction of mesoscale vortices in the Lofoten Basin based on the GLORYS database. *Russian Journal of Earth Sciences*, *20*, ES2002. https://doi.org/10.2205/2020ES000694

Fraser, R., Palmer, M., Roberts, C., Wilson, C., Copsey, D., & Zanna, L. (2019). Investigating the predictability of North Atlantic sea surface height. *Climate Dynamics*, *53*(3–4), 2175–2195. https://doi.org/10.1007/s00382-019-04814-0

Fujii, Y., Tsujino, H., Usui, N., Nakano, H., & Kamachi, M. (2008). Application of singular vector analysis to the Kuroshio large meander. *Journal of Geophysical Research*, *113*(C7). https://doi.org/10.1029/2007jc004476

Harrison, C. S., Siegel, D. A., & Mitarai, S. (2013). Filamentation and eddy−eddy interactions in marine larval accumulation and transport. *Marine Ecology Progress Series*, *472*, 27–44. https://doi.org/10.3354/meps10061

Huang, X., & Wang, G. (2022). Response of a mesoscale dipole eddy to the passage of a tropical cyclone: A case study using satellite observations and numerical modeling. *Remote Sensing*, *14*(12), 2865. https://doi.org/10.3390/rs14122865

Janjic, T., Bormann, N., Bocquet, M., Carton, J. A., Cohn, S. E., Dance, S. L., et al. (2018). On the representation error in data assimilation. *Quarterly Journal of the Royal Meteorological Society*, *144*(713), 1257–1278. https://doi.org/10.1002/qj.3130

Jiang, L., Duan, W., & Liu, H. (2022). The most sensitive initial error of sea surface height anomaly forecasts and its implication for target observations of mesoscale eddies. *Journal of Physical Oceanography*, *52*(4), 723–740. https://doi.org/10.1175/JPO-D-21-0200.1

Jiang, L., Duan, W., Wang, H., Liu, H., & Tao, L. (2023). Evaluation of the sensitivity on mesoscale eddy associated with the sea surface height anomaly forecasting in the Kuroshio Extension. *Frontiers in Marine Science*, *10*, 1097209. https://doi.org/10.3389/fmars.2023.1097209

Liu, T., & Abernathey, R. (2023). A global Lagrangian eddy dataset based on satellite altimetry. *Earth System Science Data*, *15*(4), 1765–1778. https://doi.org/10.5194/essd-15-1765-2023

Liu, T., Abernathey, R., Sinha, A., & Chen, D. (2019). Quantifying Eulerian eddy leakiness in an idealized model. *Journal of Geophysical Research: Oceans*, *124*(12), 8869–8886. https://doi.org/10.1029/2019JC015576

Lumban-Gaol, J., Leben, R. R., Vignudelli, S., Mahapatra, K., Okada, Y., Nababan, B., et al. (2017). Variability of satellite-derived sea surface height anomaly, and its relationship with Bigeye tuna (Thunnus obesus) catch in the Eastern Indian Ocean. *European Journal of Remote Sensing*, *48*(1), 465–477. https://doi.org/10.5721/EuJRS20154826

Miao, Y., Zhang, X., Li, Y., Zhang, L., & Zhang, D. (2023). Monthly extended ocean predictions based on a convolutional neural network via the transfer learning method. *Frontiers in Marine Science*, *9*. https://doi.org/10.3389/fmars.2022.1073377

Mu, M. (2013). Methods, current status, and prospect of targeted observation. *Science China Earth Sciences*, *56*(12), 1997–2005. https://doi.org/10.1007/s11430-013-4727-x

Mu, M., Duan, W., & Wang, B. (2003). Conditional nonlinear optimal perturbation and its applications. *Nonlinear Processes in Geophysics*, *10*(6), 493–501. https://doi.org/10.5194/npg-10-493-2003

Mu, M., Feng, R., & Duan, W. (2017). Relationship between optimal precursors for Indian Ocean Dipole events and optimally growing initial errors in its prediction. *Journal of Geophysical Research: Oceans*, *122*(2), 1141–1153. https://doi.org/10.1002/2016JC012527

Ni, Q., Zhai, X., Wang, G., & Hughes, C. (2020). Widespread mesoscale dipoles in the global ocean. *Journal of Geophysical Research: Oceans*, *125*(10), e2020JC016479. https://doi.org/10.1029/2020JC016479

Nicholls, R. J., & Cazenave, A. (2010). Sea-level rise and its impact on coastal zones. *Science*, *328*(5985), 1517–1520. https://doi.org/10.1126/science.1185782

Oke, P. R., Sakov, P., Cahill, M. L., Dunn, J. R., Fiedler, R., Griffin, D. A., et al. (2013). Towards a dynamically balanced eddy-resolving ocean reanalysis: BRAN3. *Ocean Modelling*, *67*, 52–70. https://doi.org/10.1016/j.ocemod.2013.03.008

Pidcock, R., Martin, A., Allen, J., Painter, S. C., & Smeed, D. (2013). The spatial variability of vertical velocity in an Iceland basin eddy dipole. *Deep Sea Research Part I: Oceanographic Research Papers*, *72*, 121–140. https://doi.org/10.1016/j.dsr.2012.10.008

Qin, X., Duan, W., & Mu, M. (2013). Conditions under which CNOP sensitivity is valid for tropical cyclone adaptive observations. *Quarterly Journal of the Royal Meteorological Society*, *139*(675), 1544–1554. https://doi.org/10.1002/qj.2109

Rayleigh, L. (1880). On the stability, or instability, of certain fluid motions. *Proceedings of the London Mathematical Society*, *S1–11*(11), 57–72. https://doi.org/10.1112/plms/s1-11.1.57

Snyder, C. (1996). Summary of an informal workshop on adaptive observations and FASTEX. *Bulletin of the American Meteorological Society*, *77*(5), 953–961. https://doi.org/10.1175/1520-0477-77.5.953

Song, T., Han, N., Zhu, Y., Li, Z., Li, Y., Li, S., & Peng, S. (2021). Application of deep learning technique to the sea surface height prediction in the South China Sea. *Acta Oceanologica Sinica*, *40*(7), 68–76. https://doi.org/10.1007/s13131-021-1735-0

Tanajura, C. A. S., Lima, L. N., & Belyaev, K. P. (2015). Assimilation of satellite surface-height anomalies data into a hybrid coordinate ocean model (HYCOM) over the Atlantic Ocean. *Oceanology*, *55*(5), 667–678. https://doi.org/10.1134/s0001437015050161

Tsujino, H., Usui, N., & Nakano, H. (2006). Dynamics of Kuroshio path variations in a high-resolution general circulation model. *Journal of Geophysical Research*, *111*(C11). https://doi.org/10.1029/2005jc003118

Wang, H., Qiu, B., Liu, H., & Zhang, Z. (2023). Doubling of surface oceanic meridional heat transport by non-symmetry of mesoscale eddies. *Nature Communications*, *14*(1), 5460. https://doi.org/10.1038/s41467-023-41294-7

Wang, Q., Mu, M., & Dijkstra, H. A. (2013). The similarity between optimal precursor and optimally growing initial error in prediction of Kuroshio large meander and its application to targeted observation. *Journal of Geophysical Research: Oceans*, *118*(2), 869–884. https://doi.org/10.1002/jgrc.20084

Weiss, J. B., & Grooms, I. (2017). Assimilation of ocean sea-surface height observations of mesoscale eddies. *Chaos*, *27*(12), 126803. https://doi.org/10.1063/1.4986088

Wu, C. C., Chen, J. H., Lin, P. H., & Chou, K. H. (2007). Targeted observations of tropical cyclone movement based on the adjoint-derived sensitivity steering vector. *Journal of the Atmospheric Sciences*, *64*(7), 2611–2626. https://doi.org/10.1175/JAS3974.1

Wu, C. C., Chen, J. H., Majumdar, S. J., Peng, M. S., Reynolds, C. A., Aberson, S. D., et al. (2009). Intercomparison of targeted observation guidance for tropical cyclones in the northwestern Pacific. *Monthly Weather Review*, *137*(8), 2471–2492. https://doi.org/10.1175/2009MWR2762.1

Yang, L., Duan, W., & Wang, Z. (2023). An approach to refining the ground meteorological observation stations for improving PM2.5 forecasts in Beijing-Tianjin-Hebei region. *Geoscientific Model Development*, *16*(13), 3827–3848. https://doi.org/10.5194/gmd-16-3827-2023

Zhang, Y., Chen, X., & Dong, C. (2019). Anatomy of a cyclonic eddy in the Kuroshio extension based on high-resolution observations. *Atmosphere*, *10*(9), 553. https://doi.org/10.3390/atmos10090553